

The importance of calorimetry for highly-boosted jet substructure

**Evan Coleman,^a Marat Freytsis,^b Andreas Hinzmann,^c Meenakshi Narain,^a
Jesse Thaler,^d Nhan Tran,^e Caterina Vernieri^e**

^a*Brown University, Providence, RI 02912, USA*

^b*Institute of Theoretical Science, University of Oregon, Eugene, OR 97403, USA*

^c*University of Hamburg, Hamburg, Germany*

^d*Center for Theoretical Physics, Massachusetts Institute of Technology, Cambridge, MA 02139, USA*

^e*Fermi National Accelerator Laboratory, Batavia, IL 60510, USA*

E-mail: evan_a_coleman@brown.edu, andreas.hinzmann@cern.ch,
freytsis@uoregon.edu, meenakshi_narain@brown.edu, jthaler@mit.edu,
ntran@fnal.gov, cvernier@fnal.gov

ABSTRACT: Jet substructure techniques are playing an essential role in exploring the TeV scale at the Large Hadron Collider (LHC), since they facilitate the efficient reconstruction and identification of highly-boosted objects. Both for the LHC and for future colliders, there is a growing interest in using jet substructure methods based only on charged-particle information. The reason is that silicon-based tracking detectors offer excellent granularity and precise vertexing, which can improve the angular resolution on highly-collimated jets and mitigate the impact of pileup. In this paper, we assess how much jet substructure performance degrades by using track-only information, and we demonstrate physics contexts in which calorimetry is most beneficial. Specifically, we consider five different hadronic final states— W bosons, Z bosons, top quarks, light quarks, gluons—and test the pairwise discrimination power with a multi-variate combination of substructure observables. In the idealized case of perfect reconstruction, we quantify the loss in discrimination performance when using just charged particles compared to using all detected particles. We also consider the intermediate case of using charged particles plus photons, which provides valuable information about neutral pions. In the more realistic case of a segmented calorimeter, we assess the potential performance gains from improving calorimeter granularity and resolution, comparing a CMS-like detector to more ambitious future detector concepts. Broadly speaking, we find large performance gains from neutral-particle information and from improved calorimetry in cases where jet mass resolution drives the discrimination power, whereas the gains are more modest if an absolute mass scale calibration is not required.

Contents

1	Introduction	1
2	General study strategy	2
2.1	Parton shower samples	3
2.2	Jet substructure observables	4
2.2.1	Mass observables	5
2.2.2	Shape observables	6
2.3	Multivariate analysis	7
3	Performance impact of neutral-particle information	7
3.1	W jets vs. quark jets	8
3.2	W jets vs. Z jets	10
3.3	Quark jets vs. gluon jets	10
3.4	Summary of truth-level study	11
4	Performance impact of improved calorimetry	12
4.1	Detector configurations	13
4.2	Results using all particles	16
4.3	Results using partial information	18
4.4	Summary of detector study	18
5	Conclusions and outlook	21
A	Top jets vs. gluon jets	23

1 Introduction

Current multipurpose detectors for hadron collider experiments [1, 2] are performing very well at reconstructing final states at unprecedented energies while operating in a challenging environment of high instantaneous luminosities. This is vital for probing rare and highly-energetic processes that are potentially sensitive to new physics. Exploring the multi-TeV regime in search of new phenomena related to the W , Z , and Higgs bosons, as well as to the top quark, represents one of the most important goals of the Large Hadron Collider (LHC) and future higher-energy colliders. The success of current and future detectors requires advanced techniques to reconstruct highly-boosted ($p_T \gg m$) heavy Standard Model (SM) objects. As objects become more energetic, their decay products become increasingly collimated, making

it difficult to detect individual particles and resolve event structure with proper resolution. The tools provided by recent developments in jet substructure [3–7] are particularly important in exploring these physical signatures at extreme kinematics [8–12].

The main features of a multipurpose detector are a strong magnetic field, a high-quality tracking system, a layered muon detection system, a high-resolution and highly-granular electromagnetic calorimeter (ECAL), and a hermetic hadronic calorimeter (HCAL). For jet substructure, in some cases, track-only observables have been exploited that only use information provided by charged particles. Compared to calorimetric objects, tracks have the advantage of being more robust to pileup (multiple collisions per bunch crossing), and they typically exhibit better angular and low-to-intermediate momentum resolution as well as lower momentum thresholds. Track-based observables have been used for example in LHC studies and measurements [13–23], and they have also been discussed in the context of future high-energy colliders [24–26].

This paper presents a two-fold exploration of the important impact that neutral-particle information and calorimeter sub-detectors can have on jet substructure reconstruction. Both of these studies use hadronic object identification as a benchmark, assessing the pairwise discrimination power between five different jet categories: boosted hadronic W bosons (W), boosted hadronic Z bosons (Z), boosted top quarks (t), light quarks (q), and gluons (g). First, we quantify the truth-level discrimination power that is lost when neutral-particle information is reduced or ignored. Then, we perform a detector-level study with three different detector simulations, where calorimeter granularity is steadily increased compared to a CMS-like configuration. The goal of both analyses is to understand the technological demands on future detectors if we wish to fully exploit jet substructure information and maximize the physics potential of colliders beyond the LHC.

The rest of this paper is organized as follows. In Sec. 2, we discuss the general strategy of the study, including the event generator samples, the choice of jet substructure observables, and the setup to build multivariate jet discriminants. We present our truth-level study of neutral-particle information in Sec. 3, and we discuss the impact on neutral object reconstruction of different calorimeter scenarios in Sec. 4. We conclude in Sec. 5 with a summary of our findings, and we discuss the implications for current physics analyses and future detector designs.

2 General study strategy

In jet substructure, one studies the products of hadronic fragmentation and decays, consisting primarily of charged and neutral hadrons. Charged hadron reconstruction benefits from precision tracking detectors, though they are limited at the highest energies. Neutral pions, which decay promptly to photon pairs, are reconstructed by the ECAL; it provides excellent energy resolution and can detect photons with moderate angular resolution thanks to the relatively narrow Molière radius for photons. Other neutral hadrons (as well as charged hadrons) are detected through hadronic showers in the HCAL, which exhibit a broad angular profile from

nuclear interactions. In this study, we adopt the philosophy of particle-flow reconstruction, where information from all sub-detectors are correlated to identify and reconstruct each final-state particle, allowing one to, for example, disentangle charged and neutral hadrons in the HCAL. Particle-flow was first developed and used by the ALEPH experiment at LEP [27] and is currently in use at the LHC [28, 29].

Due to isospin considerations, jets on average consist of 60% charged hadrons, 30% photons (from neutral pion decay), and 10% neutral hadrons,¹ although these fractions are subject to large jet-by-jet fluctuations [28, 29]. Because charged hadrons are the dominant jet component and because neutral hadrons suffer from the poor angular resolution of the HCAL, this has led to the study of track-only observables in jet substructure [13–26]. At a high-luminosity collider, a key advantage of using only tracks is that precise vertexing can be used to achieve minimal contamination from pileup collisions. On the other hand, jet-to-jet fluctuations of charged content cause the distributions of track-only observables to be intrinsically wider than those based on all particles; this in turn leads to reduced discrimination power in the context of jet substructure.

The aim of this paper is to quantify the degree to which neutral information is needed for discrimination tasks using jet substructure (Sec. 3), and then determine the calorimeter performance required to improve upon tracker-only information (Sec. 4). Both studies rely on the same parton shower generator tools, described in Sec. 2.1, and the same suite of jet substructure observables, listed in Sec. 2.2. We use a multivariate analysis to construct optimal discriminators for various jet types, as detailed in Sec. 2.3, and we use ROC (Receiver-Operator Characteristic) curves to quantify the discrimination power under different neutral-particle and calorimeter-performance scenarios. For consistency, we adopt the convention that signal-background pairs are always arranged in the hierarchy $W \rightarrow Z \rightarrow t \rightarrow q \rightarrow g$, such that e.g. W samples are always treated as signal and g samples are always treated as a background.

2.1 Parton shower samples

Events samples are generated both at a proton-proton center-of-mass energy of $\sqrt{s} = 100$ TeV to model a future collider and at $\sqrt{s} = 13$ TeV for comparisons to LHC performance. For both energies, parton-level W^+W^- , ZZ , $t\bar{t}$, $q\bar{q}$, and gg events are first produced at leading-order using MADGRAPH5_AMC@NLO [30] (version 2.3.1) with the NNPDF23LO1 parton distribution functions (PDFs) [31]. In order to focus on a relatively narrow kinematic range, the transverse momenta of the partons and undecayed gauge bosons are generated in window with $\delta p_T/p_T = 0.01$, centered at 1 TeV for $\sqrt{s} = 13$ TeV and at $p_T = 5$ TeV for $\sqrt{s} = 100$ TeV. These parton-level events are then decayed and showered in PYTHIA8 [32] (version 8.212) with the Monash 2013 tune [33], including the contribution from the underlying event. For each p_T bin and final state, 200,000 events are generated.

¹These fractions are approximate and depend more specifically on color and flavor structures, hadronization dynamics, and detector momentum thresholds.

Mass observables	Shape observables
m_{plain}	$\tau_{N=1,2,3}^{\beta=1,2}$
m_{prun}	$\tau_{21}^{\beta=1,2}$
m_{trim}	$\tau_{32}^{\beta=1,2}$
m_{mMDT}	$C_{N=1,2}^{\beta=1,2}$
$m_{\text{SD}}^{\beta=1,2}$	$D_2^{\beta=1,2}$
	p_{T}^D
	$\sum z \log z$
	Multiplicity

Table 1: A summary of the observables used in the analysis, roughly divided into mass-like and shape-like categories.

We implement a variety of jet recombination algorithms and substructure tools via the FASTJET 3.1.3 and FASTJET CONTRIB 1.027 packages [34, 35]. As a baseline, all jets are clustered using the anti- k_{T} algorithm [36], with a distance parameter of $R = 0.8$. Even though the parton-level p_{T} distribution is narrow, the jet p_{T} spectrum is significantly broadened by kinematic recoil from the parton shower and energy migration in and out of the jet cone. We apply a cut on the reconstructed jet p_{T} to remove extreme events from the analysis, vetoing those outside a window of $0.8 \text{ TeV} < p_{\text{T}} < 1.6 \text{ TeV}$ for the $p_{\text{T}} = 1 \text{ TeV}$ bin and $4.5 \text{ TeV} < p_{\text{T}} < 6 \text{ TeV}$ for the $p_{\text{T}} = 5 \text{ TeV}$ bin.

2.2 Jet substructure observables

The jet substructure community has developed a wide variety of observables to identify the origin of a jet based on the structure of its radiation pattern. We focus on $W/Z/t/q/g$ discrimination. The Higgs boson, decaying to a bottom quark pair, is excluded as its mass and substructure are quite similar to W and Z bosons, and Higgs-tagging relies heavily also on the identification of bottom quarks and secondary vertex reconstruction, which we do not pursue here. The goal of this study is not to implement an exhaustive jet substructure catalog, but rather focus on the *change* in discrimination power from adding neutral or calorimeter information. That said, by combining several observables together into a multivariate discriminant (see Sec. 2.3), one can achieve excellent tagging identification for each pairwise discrimination task, and we do not expect the qualitative lessons from this study to change substantially by adding more jet observables.

In Table 1, we list all the observables used in this study, making a distinction between “mass” and “shape” observables. This label denotes a conceptual difference between mass-like observables, which are sensitive to the absolute energy scale of the jet (dimensionful), and shape-like observables, which are sensitive to relative energy scales within the jet (dimension-

less). This distinction is important for interpreting the results of this study since calorimetry is most important in cases where mass resolution drives the discrimination power. That said, a strict distinction between these observable types is not well-defined since there are some “mass-like” shape observables (e.g. $C_1^{\beta=2}$). Moreover, because we are working with jet samples in relatively narrow p_T ranges, this blurs the distinction between dimensionful and dimensionless quantities. If we wanted to have fully orthogonal sets of information, we would have to carefully decorrelate shape-like from mass-like information as in Ref. [37, 38], which we do not pursue here. When showing results, we define discriminants which use only mass-like observables and then also define discriminants for mass- plus shape-like observables as is typically used in LHC analyses.

2.2.1 Mass observables

- **Jet mass:** The resonance mass of W/Z bosons and t quarks sets an intrinsic jet mass scale, which is unlike a typical q/g jet, such that mass can be used as a primary discriminant between $W/Z/t/q/g$ jets. The bulk of the W/Z (t) jet mass arises from the kinematics of the two (three) jet cores that correspond to the two (three) prongs. By contrast, the q/g jet mass arises mostly from soft gluon radiation, with the average mass proportional to the Casimir factor (4/3 for quarks, 3 for gluons).
- **Groomed jet mass:** Jet grooming methods such as trimming (m_{trim}) [39], pruning (m_{prun}) [40], modified mass drop [7, 41] (m_{mMDT}), and soft drop [42] (m_{SD}^β) help remove soft and wide-angle radiation from the jet cone. Grooming reduces the jet mass of q/g jets by an $\mathcal{O}(1)$ factor, while affecting $W/Z/t$ jets less and grooming them closer to their expected intrinsic mass value. We use each of the grooming methods above to compute the groomed jet mass. For soft drop, we compare different values of the angular exponent β in the soft-drop condition. We use $\beta = 0$, which corresponds to the modified mass drop procedure ($m_{\text{mMDT}} = m_{\text{SD}}^{\beta=0}$) as well as $\beta = 1, 2$, all with $z_{\text{cut}} = 0.1$. The trimmed mass is computed using $r_{\text{trim}} = 0.2$ and $z_{\text{trim}} = 0.05$. The pruned mass is computed setting the soft radiation fraction to $z = 0.15$ and internal mass selection at $r_0 = 0.5$.

In cases where only partial jet information is used for a (groomed) jet mass observable, we rescale it by the total energy of the jet:²

$$m_{\text{reported}} = m_{\text{partial}} \frac{E_{\text{total}}}{E_{\text{partial}}}. \quad (2.1)$$

This corresponds to a jet reconstruction strategy where the total jet energy is known but its substructure is determined from only partial information. In the case of track-only measurements, this procedure is sometimes referred to as track-assisted mass [17, 23–26], which not only reduces the bias from charged-to-neutral fluctuations but also improves the resolution on the mass. This is a sensible strategy even with a coarse HCAL, since determining E_{total} does

²Very similar behavior would have been obtained from rescaling by the total jet p_T instead.

not require good angular resolution, only good energy resolution. In the discussion below, when referring to “track-only” or “track-plus-photon” observables, we are always implicitly including this rescaling factor.

2.2.2 Shape observables

- **N-subjettiness:** The N -subjettiness observable τ_N quantifies how consistent a jet is with having N or more subjets [43]. After identifying N subjet axes, τ_N is computed as the p_T -weighted distance between each jet constituent and its nearest subjet axis. Two different angular exponents are considered in this study: $\beta = 1, 2$. The ratio $\tau_{21}^\beta \equiv \tau_2^\beta / \tau_1^\beta$ yields considerable separation between W/Z jets and q/g jets. The ratio $\tau_{32}^\beta \equiv \tau_3^\beta / \tau_2^\beta$ is similarly used to identify top quarks. To aid in q/g discrimination, individual $\tau_{N=1,2,3}^\beta$ components are also included in this study, although we do not include the case of the Les Houches Angularity with $N = 1$, $\beta = 0.5$ [44]. In all cases, the subjet axes are determined using one-pass k_T optimization [45].
- **Energy correlation functions:** The observables C_i^β [46] and D_i^β [47] can identify N -prong jet substructure without requiring a subjet finding procedure, only using information about the energies and pairwise angles of particles within a jet. Here, C_i^β and D_i^β are ratios involving up to $(i + 1)$ -point correlation functions, and β is again an angular exponent for the pairwise particle distances. In a typical application, C_1^β is used for q/g discrimination while C_2^β and D_2^β are used to identify W/Z bosons. In this study, we consider $\beta = 1, 2$, and we do not include more general energy correlation functions like $N_{i=2,3}^\beta$ [48]. We also include the infrared and collinear unsafe case of C_1^β with $\beta = 0$, which has the same discrimination power as p_T^D [49, 50]. Of course, including more correlators could further aid in $W/Z/t/q/g$ separation—e.g. $\beta = 0.5$ or 0.2 is known to improve q/g separation for C_i^β [46] and there are powerful four-point correlator combinations like D_3^β [51]—but we do not expect them to make a qualitative difference to this study.
- **$\sum \mathbf{z} \log \mathbf{z}$:** The fraction of energy carried away by daughter particles within a jet, $z_i = E_i/E_{\text{parent}}$, is a measure of jet softness, and can be used to separate quark from gluon jets. Following Ref. [52], we consider a sum over the jet constituents of $\sum_i z_i \log z_i$. In cases where only partial information is used, we define E_{parent} using the reduced information such that $\sum_i z_i = 1$.
- **Hadron multiplicity:** The number of jet constituents is powerful both for q/g discrimination and for discriminating color singlet jets like W/Z bosons versus colored objects like q/g (see e.g. [13, 16, 18, 52–54]).

To avoid a proliferation of observables, we decided to compute all of the shape observables without applying any jet grooming techniques. It is known that grooming can fundamentally alter the discrimination power of shape observables [48, 55], though we do not expect the

relative gains in including neutral or calorimeter information to be much affected by including groomed jet shapes.

2.3 Multivariate analysis

To quantify the discrimination power of the above mass and shape observables, a boosted decision tree (BDT) classifier is trained for discriminating each pair of jet sample types. This discriminator is close to optimal (given the information provided), allowing us to de-emphasize the power of any single observable and focus on the combined performance for a given level of neutral or calorimeter information.

The multivariate analysis is implemented via the TMVA package [56]. The resulting BDT forest is composed of 50 trees, each with a maximum depth of 10 branches and at most, 10^6 nodes. We apply a variety of techniques to improve the decision quality of the classifier and prevent overtraining, including gradient boosting [57]. More powerful multivariate and jet imaging techniques may be somewhat better in performance [58], though in practice, most gains over a BDT approach are at the level of 10–20% [59, 60].

Part of the output of the BDT is a pair of distributions taking values from -1 to 1 , one for the signal-type jet and one for the background-type jet in the training. These distributions are used to quantify our ability to discriminate between pairs of SM objects. The primary way we illustrate discrimination power is through ROC curves, which plot the background efficiency for a given signal efficiency. Here, the signal efficiency (ϵ_{sig}) is the cumulative density of one of the two distributions, which we label $f_s(t)$,

$$\epsilon_{\text{sig}} = \int_{-1}^x dt f_s(t), \quad (2.2)$$

and the background efficiency (ϵ_{bkg}) is the same integral over the other distribution, $f_b(t)$.

3 Performance impact of neutral-particle information

In this section, we quantify the gains in jet substructure discrimination performance from including neutral-particle information compared to using only track-based observables. We consider three different categories of particles to calculate the mass- and shape-like observables from Sec. 2.2: (i) charged particles only, “tracks”, (ii) charged particles plus photons, “tracks+ γ ”, and (iii) all particle types, “all particles”. These categories roughly map onto the information available in (i) just the tracker, (ii) the tracker plus ECAL, and (iii) the whole detector. We emphasize, however, that this is a truth-particle-level study; the impact of detector configurations is considered in Sec. 4.

For our study, we considered all pairwise discrimination tasks for $W/Z/t/q/g$ jets, for a total of ten different binary BDT classifiers. We also performed separate studies on two p_T regimes: 1 TeV (at a 13 TeV machine) and 5 TeV (at a 100 TeV machine). Given the many permutations, we focus our narrative on three tasks— W vs. q , W vs. Z , and q vs. g —since they capture well the differing impact of neutral-particle information. Specifically, W vs. q

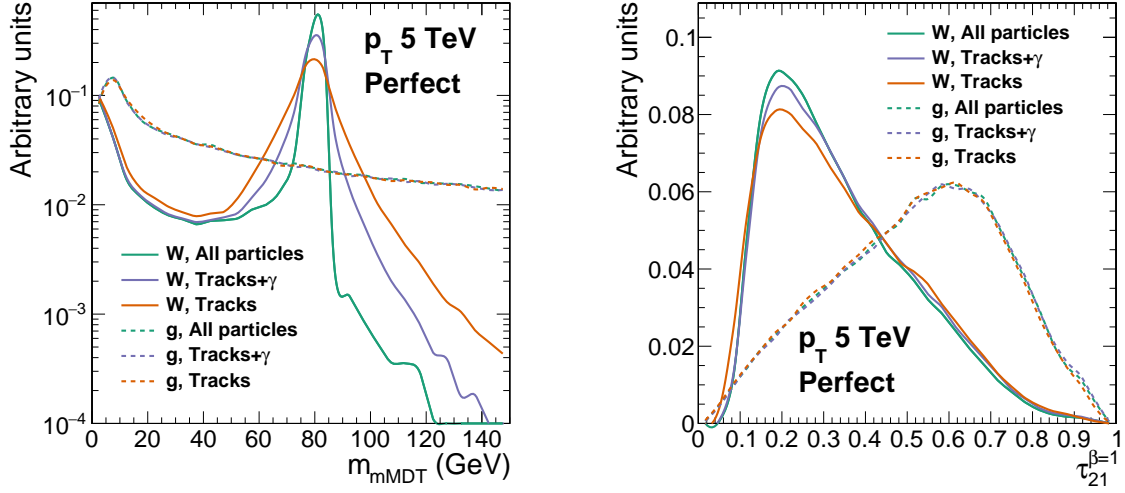


Figure 1: Distributions of (left) m_{mMDT} and (right) $\tau_{21}^{\beta=1}$ for W jets and gluon-initiated jets in the 5 TeV p_T bin. Three different particle categories are considered to calculate these observables: tracks, tracks+ γ and all particles, as defined in the text.

discrimination depends on both mass and shape observables; W vs. Z is affected primarily by mass observables; and q vs. g exploits mostly shape observables. Additional comparisons including top jets are in App. A.

In Fig. 1, we show example distributions of m_{mMDT} and $\tau_{21}^{\beta=1}$ obtained from the W and gluon parton shower samples from Sec. 2.1, assuming a perfect detector. Immediately one notices the differing role that neutral-particle information plays for mass-like compared to shape-like observables. For the W sample with an intrinsic mass scale, the groomed mass resolution degrades quickly in going from all particle information to just tracks. By contrast, the N -subjettiness shape information is much more stable as the level of neutral information is diminished. These features will be reflected in the ROC curves below.

3.1 W jets vs. quark jets

We begin by comparing W jet versus quark jet discrimination using different degrees of neutral-particle information. In Fig. 2, the ROC discrimination curves are reported as W jet tagging efficiency versus quark jet tagging efficiency for BDT discriminants built on just mass observables and, separately, on all observables (i.e. mass plus shape). The reason we do not show a BDT from just shape observables is twofold: first, almost all jet substructure analyses use mass as part of their discrimination strategies; and second, as discussed in Sec. 2.2, shape observables like $C_1^{\beta=2}$ are highly correlated with mass when considering a narrow p_T bin.

As more neutral particle information is added, we see that W/q discrimination power is indeed improved. This is expected for mass-only observables, since, as already seen in the left panel of Fig. 1, the W boson mass resolution improves as photons and neutral hadrons

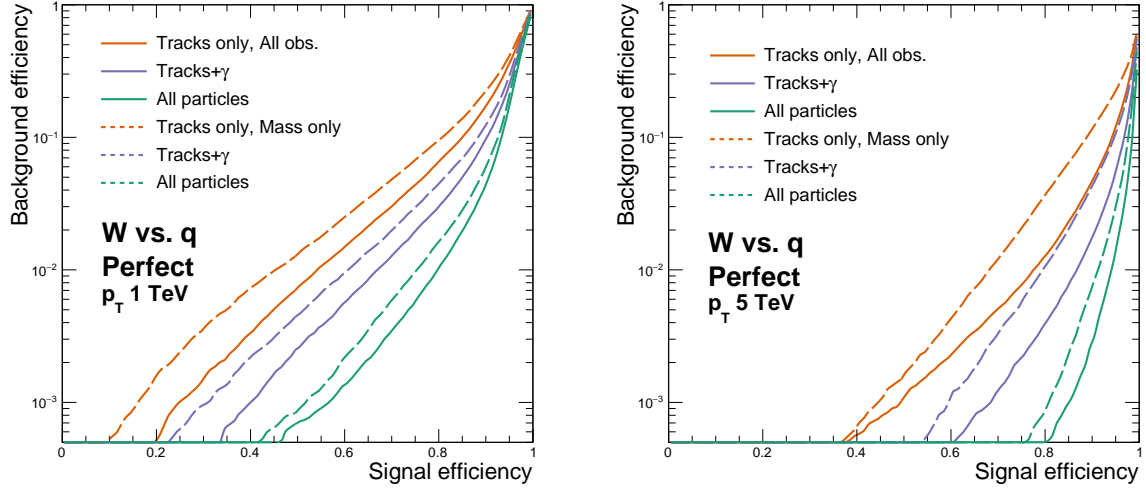


Figure 2: ROC discrimination curves for the (left) 1 TeV and (right) 5 TeV p_T bins. W -tagging (signal) versus q -tagging (background) efficiencies are shown for (dashed) mass and (solid) mass-plus-shape observables, and for three different particle categories: tracks, tracks+ γ and all particles. Here, a perfect detector is assumed.

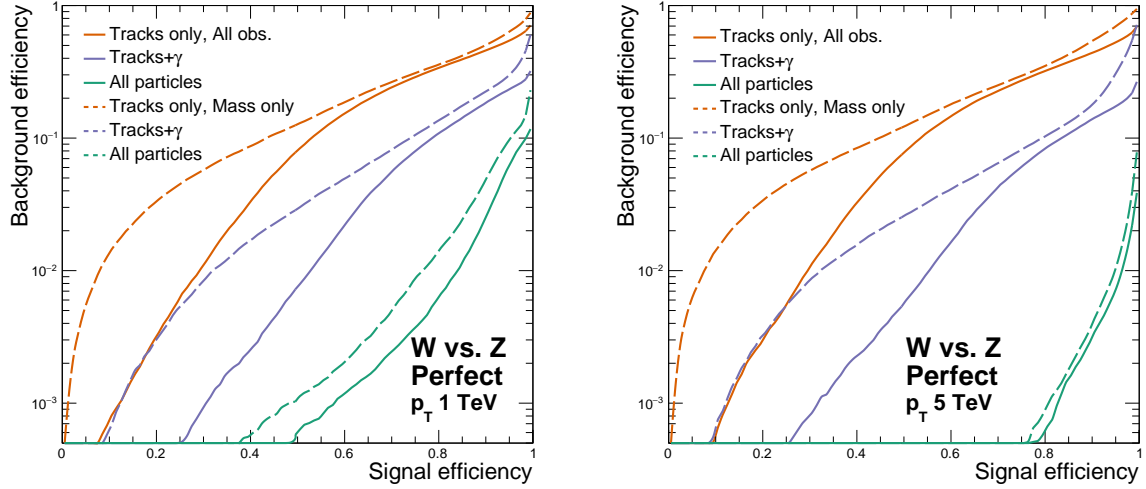


Figure 3: Same as Fig. 2, but for W jets (signal) versus Z jets (background).

are included. Since W bosons and quark jets have different prong-like structures, shape information provides additional discrimination power beyond just mass. However, the *relative* improvement offered by shape information does not improve as neutral information is added, since charged particles already provide substantial information on the overall jet topology.

Finally, in comparing the left (1 TeV) and right (5 TeV) panels of Fig. 2, one sees that the overall discrimination power increases at higher p_T . This is expected, at least when assuming a perfect detector, since more energetic quark jets radiate more copiously, whereas W bosons are color singlets and therefore have a fixed radiation pattern with p_T .

3.2 W jets vs. Z jets

We now turn to W jet versus Z jet discrimination. Because W and Z jets are topologically quite similar, mass resolution plays a crucial role in this task. In Fig. 3, the ROC discrimination curves are reported as W jet tagging efficiency versus Z jet tagging efficiency, using the same configurations as Fig. 2. When all particle information is included, shape information is quite subdominant to the mass information, as expected since the primary difference between W and Z is the mass peak at 80 GeV versus 91 GeV. When neutral-particle information is removed, the discrimination power degrades dramatically, though the performance can be partially recovered by supplementing mass with shape observables. As we will see below, the large separation power seen in the all-particle case cannot be realized in practice given calorimeter limitations. Still, this example shows the dramatic gains possible from neutral-particle information when mass resolution drives performance.

Note that W/Z separation improves at higher p_T when using all particles. The reason is that mass resolution can be degraded by underlying event and initial state radiation, which have a proportionally smaller impact as the jet p_T increases.

3.3 Quark jets vs. gluon jets

Our final case study is quark versus gluon tagging. In Fig. 4, the ROC discrimination curves are reported as quark jet tagging efficiency versus gluon jet tagging efficiency, using the same configurations as Fig. 2. Because there is no intrinsic mass scale for quark and gluon jets, discrimination between the two is dominated by shape information. While mass observables appear to perform well on their own, this is primarily due to the use of a narrow p_T bin, allowing the masses to be used as a proxy for the amount of radiation in the jet. The differences in the discrimination power between the different particle categories and observable sets are smaller than in the prior examples, and the discrimination power is fairly independent of p_T . With no parametric separation in phase space between quark and gluon jets [61], such similarities are expected.

Quark/gluon tagging is an example where neutral-particle information has the smallest impact since shape information about the jets can be adequately captured using only partial jet information. From a perspective of cost over performance optimization, there is a noticeable gain in going from tracks to tracks plus photons, though perhaps not much to be gained beyond that in using all particles. In cases like this where absolute discrimination

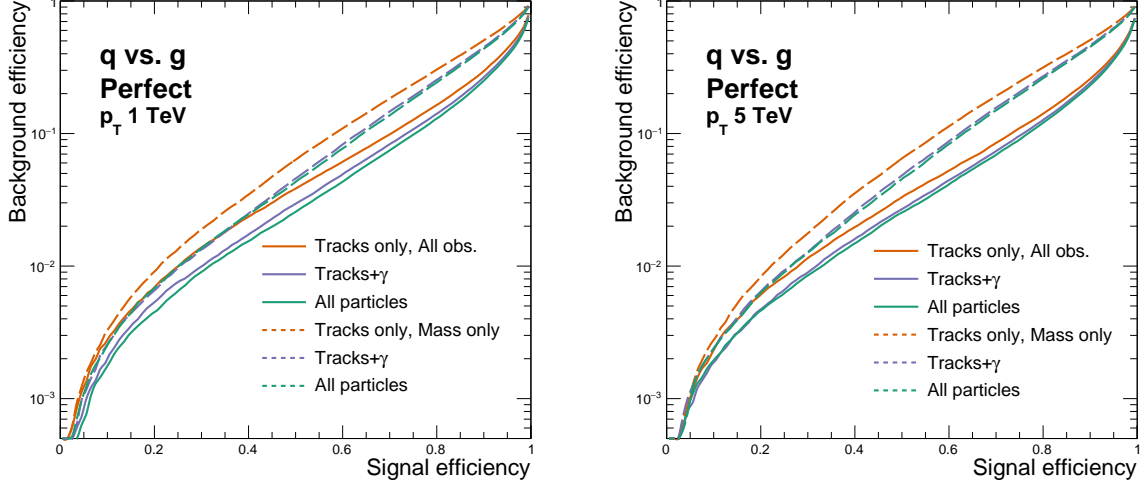


Figure 4: Same as Fig. 2, but for quark jets (signal) versus gluon jets (background).

power is fairly independent of the input particle collections, calorimeters are expected to play a subdominant role.

3.4 Summary of truth-level study

The three case studies above are just a sampling of the ten pairwise tasks we tested. It is instructive to summarize the other seven tasks, as well as summarize the gain in discrimination power when adding neutral-particle information. To do so, we compute the background rejection (i.e. one over the background efficiency) for each discriminant at an operating point with fixed signal efficiency, $S(\%)$. We then take the ratios of the background rejection factors between scenarios A and B , representing different particle categories:

$$\mathcal{R}_S = \left(\frac{\epsilon_{\text{bkg}}^A(\epsilon_{\text{sig}}^A = S(\%))}{\epsilon_{\text{bkg}}^B(\epsilon_{\text{sig}}^B = S(\%))} \right)^{-1}. \quad (3.1)$$

The ratio illustrates the performance gained (in background rejection) by adding neutral-particle information.

In Fig. 5, we display these ratios for the $p_T = 1$ (5) TeV bin for $S(\%) = 80\%$ (90%), arranged in a 5×5 matrix for each pairwise comparison of $W/Z/t/q/g$ jets. As the scenario A baseline, we take the track-only particle category. We then compare to scenario B with either tracks plus photons (lower right triangle) or all particles (upper left triangle). As expected from the case studies above, the improvement in adding neutral-particle information is marginal for quark vs. gluon jets, but is more significant for W/Z vs. q/g jets. The gains are largest when mass resolution is most important such as in W vs. Z discrimination. In all cases, using tracks+ γ yields a noticeable improvement compared to just tracks, but the gains are always better using all particle information.

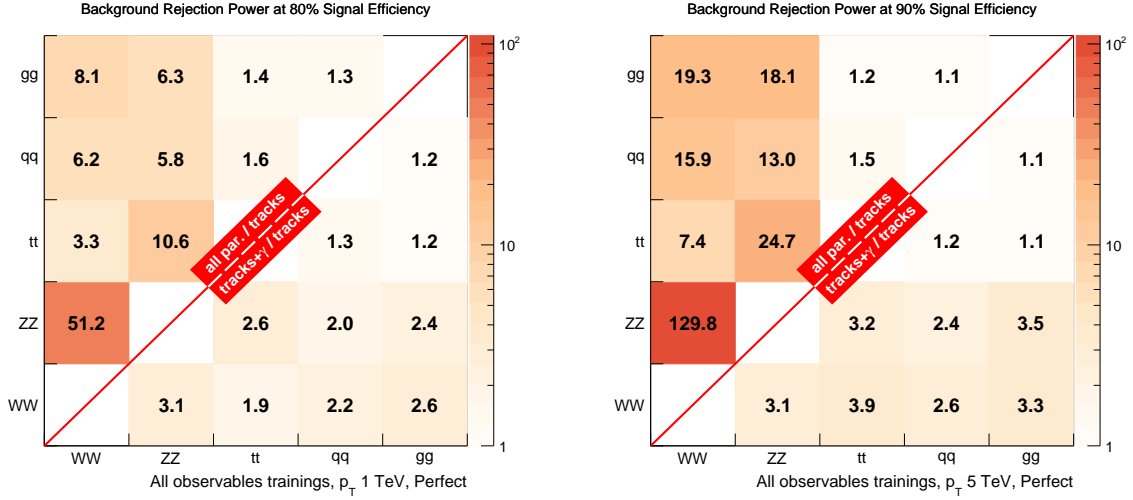


Figure 5: Background rejection ratio (left) \mathcal{R}_{80} for the $p_T = 1$ TeV bin and (right) \mathcal{R}_{90} for the $p_T = 5$ TeV bins, for all pairwise discrimination tasks among $W/Z/t/q/g$ jets, using mass-plus-shape observables and a perfect detector. Values in the lower right triangle refer to the ratio (tracks+ γ)/(tracks), while those in the upper left triangle refer to (all particle)/(tracks). All such plots in this paper share the same color scale.

When inspecting the full 5×5 discrimination matrix, we find an interesting feature in top vs. q/g jet discrimination. Contrary to naive expectations, the gains when including neutral-particle information are not as strong as in the W/Z vs. q/g cases, despite the fact that the top quark has an intrinsic mass scale. It is important to note that the top jet case is more complicated due to the colored, 3-prong nature of the top quark, and we suspect that there are two effects that render absolute mass information less relevant. The first is that the absolute mass scale for the top jet (m_{top}) is much larger than the W and Z jet cases, leading to greater baseline signal/background separation. The second is that the top jet, being colored, tends to have a worse intrinsic mass resolution compared to W/Z color singlets. This ultimately results in mass resolution being less important for top vs. q/g jet discrimination, and therefore the degradation in mass resolution from the lack of neutral-particle information is less pronounced.

4 Performance impact of improved calorimetry

The results in the previous section demonstrate the importance of neutral-particle information for hadronic jet identification at a general-purpose detector. Of course, the above analysis assumed a perfect detector, neglecting the significant degradation due to the granularity and smearing that are present in real detector systems. To place our findings in a more realistic

Scenario:	Perfect	CMS-like	Future 1	Future 2
$\sigma_{\text{HCAL}}^\eta/E = \sigma_{\text{HCAL}}^\phi/E$	0	0.022	0.01	0.002
$\sigma_{\text{ECAL}}^\eta/E = \sigma_{\text{ECAL}}^\phi/E$		0.0175	0.005	0.001
$\sigma_{\text{charged particles}}^E/E$		$0.00025 p_{\text{T}} \oplus 0.015$	$\left. \vphantom{\begin{matrix} \sigma_{\text{charged particles}}^E/E \\ \sigma_{\text{photons}}^E/E \\ \sigma_{\text{neutral hadrons}}^E/E \end{matrix}} \right\} \times \frac{1}{2}$	
$\sigma_{\text{photons}}^E/E$		$0.021/\sqrt{E} \oplus 0.094/E \oplus 0.005$		
$\sigma_{\text{neutral hadrons}}^E/E$		$0.45/\sqrt{E} \oplus 0.05$		
$E_{\text{track}}^{\text{max}}$	∞	220 GeV		

Table 2: Smearing resolutions and calorimeter granularities for the detector components in each hypothetical detector scenario. Unless otherwise specified, all quantities are dimensionless. Resolutions which depend on p_T and E are scaled with coefficients measured in GeV^a , for appropriate a .

context, we now study the effects of improved calorimeter granularity and resolution on the discrimination of $W/Z/t/q/g$ jets.

4.1 Detector configurations

We develop a custom detector simulation which reproduces the main resolution effects relevant for jet substructure reconstruction through particle level smearing and granularization described in detail below. This simulation is representative of current and future detector concepts employing particle-flow-based reconstruction, such as the CMS [28] or ATLAS [29] detectors at the LHC.

In the simulation, we first categorize the generated particles into charged particles, photons (including $\pi_0 \rightarrow \gamma\gamma$), and neutral hadrons. Tracking inefficiencies occur at high particle momenta and within high momentum jets, where the tracking detector granularity is not sufficient to reconstruct highly-collimated particles. Since both inefficiencies are correlated within high momentum jets, they are simulated together by treating charged particles with momenta above a threshold $E_{\text{track}}^{\text{max}}$ as neutral hadrons. CMS and ATLAS also have tracking inefficiencies at lower momenta and there is an ambiguity in the mapping of calorimeter deposits to charged and neutral particles which is enhanced in high-momentum jets. Those effects are not explicitly simulated, though, jet substructure reconstruction performance was found to be well-reproduced approximating all tracking-related effects with a simple $E_{\text{track}}^{\text{max}}$ threshold. The generated neutral hadrons are then discretized to simulate the spatial resolution $\sigma_{\text{CAL}}^\eta = \sigma_{\text{CAL}}^\phi$ of the ECAL and HCAL. Finally, all particles are smeared according to parametrized resolutions $\sigma_{\text{particle}}^E$ for each particle type. To match onto the study of Sec. 3, we sometimes include results for a perfect detector as well.

As a baseline, we consider a scenario that represents the future performance of the CMS detector [1]. The threshold $E_{\text{track}}^{\text{max}}$ for this scenario is chosen such that it matches the jet mass resolution at high momenta obtained from simulations of the current CMS detector [62], and then increased by a factor 2 as suggested by simulation studies for the HL-LHC Phase-II

upgrade of the CMS tracker [63]. This improvement comes from a higher granularity pixel detector which will better distinguish hits from nearby high p_T tracks. Using W and q/g jets with transverse momenta in the range of 300 GeV and 3.5 TeV, we compared the resolution in jet mass and substructure observables obtained from this scenario to CMS public results and found them to be compatible [64–66]. The W and q/g jet selection efficiencies also agree with the CMS performance, which are similar to ATLAS as well.

Beyond the CMS-like configuration, we consider two more detector scenarios, which include improved calorimeter performance as proposed for future detectors [67]. These two scenarios are summarized in Table 2 as “Future 1” (F1) and “Future 2” (F2). Both scenarios feature a factor of two improvement in the calorimeter energy resolution compared to a CMS-like configuration. The calorimeter granularity is also improved by at least a factor of two (for F1) and ten (for F2), with more significant improvements in the ECAL compared to the HCAL.

We illustrate the impact of detector performance in Fig. 6, showing (left column) m_{mMDT} and (right column) $\tau_{21}^{\beta=1}$ distributions for W and gluon jets. The various curves in each panel correspond to the three different detector configurations, while the rows correspond to different levels of neutral-particle information. Obviously, calorimeter performance has the biggest impact when neutral-particle information is used, and both the jet mass resolution and discrimination based on $\tau_{21}^{\beta=1}$ improve with the detector performance. In the W versus Z jet discrimination scenario, the effect of mass resolution is further magnified, as shown in Fig. 7. This is especially true in the case of $p_T = 5$ TeV where the improved calorimeter granularity results in a drastic improvement on the mass resolution. A key question, to be discussed further in Sec. 5, is whether the performance gains seen in the F1 and F2 configurations are sufficiently dramatic to justify their application in a future multi-purpose detector.

Both at the LHC and at future hadron colliders, pileup is an ever-present challenge that degrades jet performance. For the studies here, though, the effect of pileup is ignored. One justification for this choice is that we focus on very high p_T jets, which are less susceptible to pileup present at a significantly lower energy scales. More to the point, there are a number of pileup mitigation techniques that have been shown to greatly reduce the effects of pileup on jet substructure observables [68–72]. We, therefore, assume that the effects of pileup can be factorized from the impact of calorimeter granularity and resolution, at least for the high p_T jets studies here. To verify the above assumption about pileup, we performed a validation study where neutral energy equivalent to roughly 200 pileup collisions was injected into W jet events. (Charged pileup can be safely ignored since the vast majority of it can be removed using vertexing information.) We found that W jet tagging performance and mass resolution were negligibly affected by pileup, both for jet p_T of 1 TeV and 5 TeV. Of course, pileup is a much larger effect for more moderately boosted objects in the range of a few hundred GeV. For future work, it would be interesting to study the effect of calorimeter resolution and granularity on pileup mitigation techniques at more moderate energies.

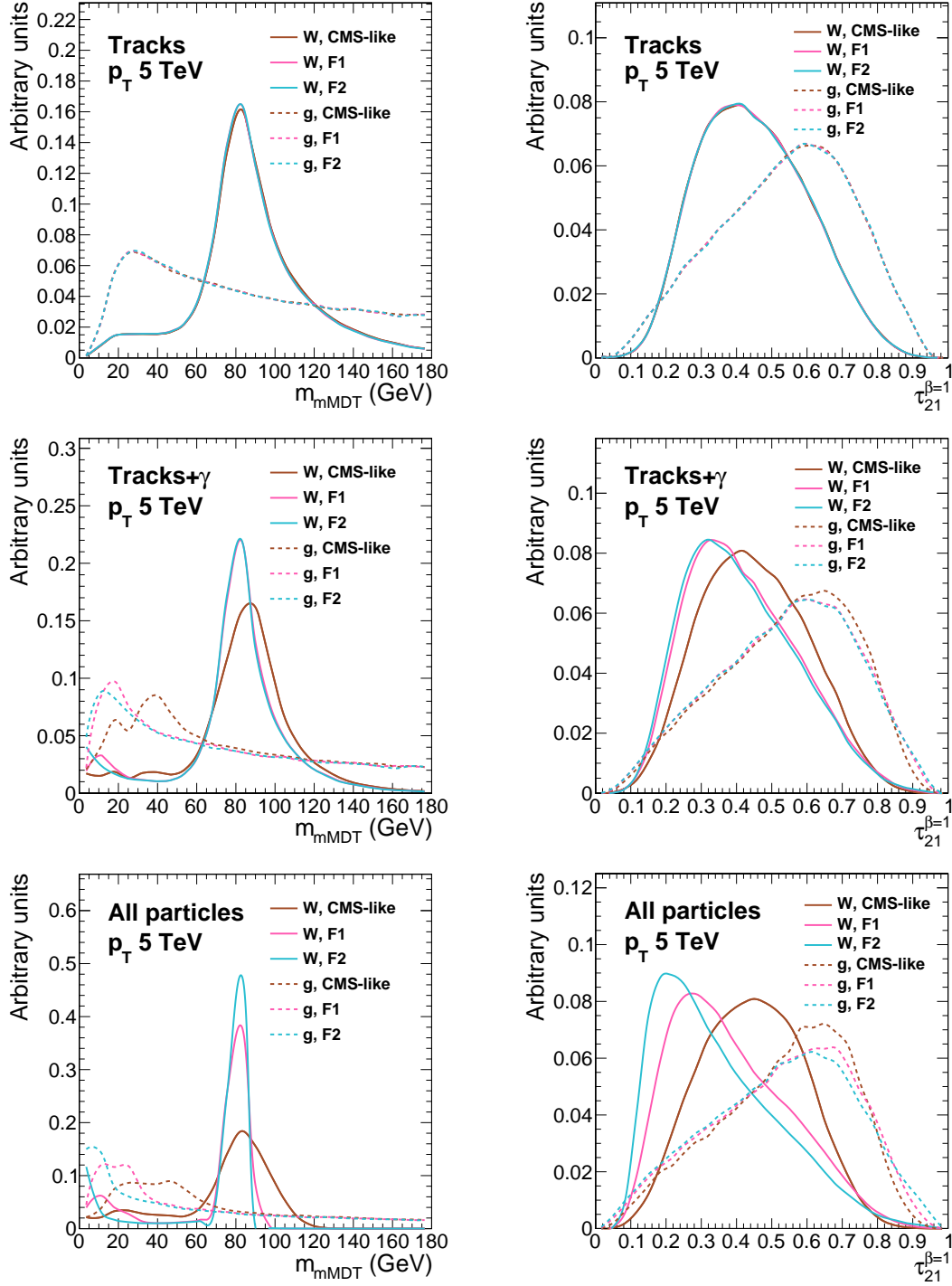


Figure 6: Distributions of (left) m_{mMDT} and (right) $\tau_{21}^{\beta=1}$ for W jets and gluon jets at $p_T = 5$ TeV in each detector configuration. From top to bottom, three different particle categories are considered: tracks, tracks+ γ , and all particles.

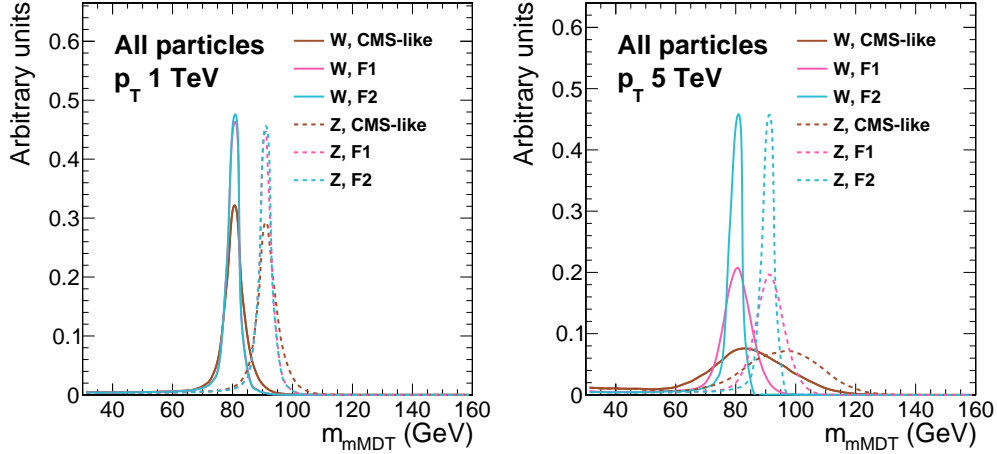


Figure 7: Distributions of m_{mMDT} for W jets and Z jets at (left) $p_T = 1$ TeV and (right) 5 TeV in each detector configuration. We consider the all particles category.

4.2 Results using all particles

At a general-purpose detector with an effective particle-flow reconstruction algorithm, it typically makes sense to use all particle information for jet substructure reconstruction. In Fig. 8, we consider the same three discrimination tasks from Sec. 3— W vs. q , W vs. Z , and q vs. g —now comparing the performance across the CMS-like, F1, and F2 detector configurations using all available information. Results are shown both for the (left column) 1 TeV and (right column) 5 TeV p_T bins. We also include perfect reconstruction for reference.

In all cases, having better detector performance improves (or maintains) discrimination power. The most (un)striking feature is that q vs. g jet separation only slightly improves with the detector performance, as could be anticipated since these are shape-based discrimination tasks which already leverage the great tracking performance. When considering W vs. q or W vs. Z discrimination, however, a sizable gain comes from using an improved detector. In the W vs. q case, where shape information is also powerful, the improvement in background rejection going from a CMS \rightarrow F1 \rightarrow F2 detector at $p_T = 5$ TeV is around a factor of 5 at a signal efficiency of 50%. This improvement can most easily be seen by looking at the Fig. 6 (bottom left) which shows the mass resolution improvement of the W jet signal. Even larger gains are seen for W vs. Z discrimination, where going from a CMS \rightarrow F2 detector results in two orders of magnitude improvement in background rejection power, again primarily because of the improved mass resolution which can be best seen in Fig. 7.

It is interesting to compare the different behaviors in the 1 TeV and 5 TeV samples. At $p_T = 1$ TeV, going from an F1 \rightarrow F2 detector shows no significant improvement for any of the discrimination tasks, whereas, at $p_T = 5$ TeV, there are still gains in going from F1 \rightarrow F2. This indicates there is an asymptotic detector granularity for a given p_T such

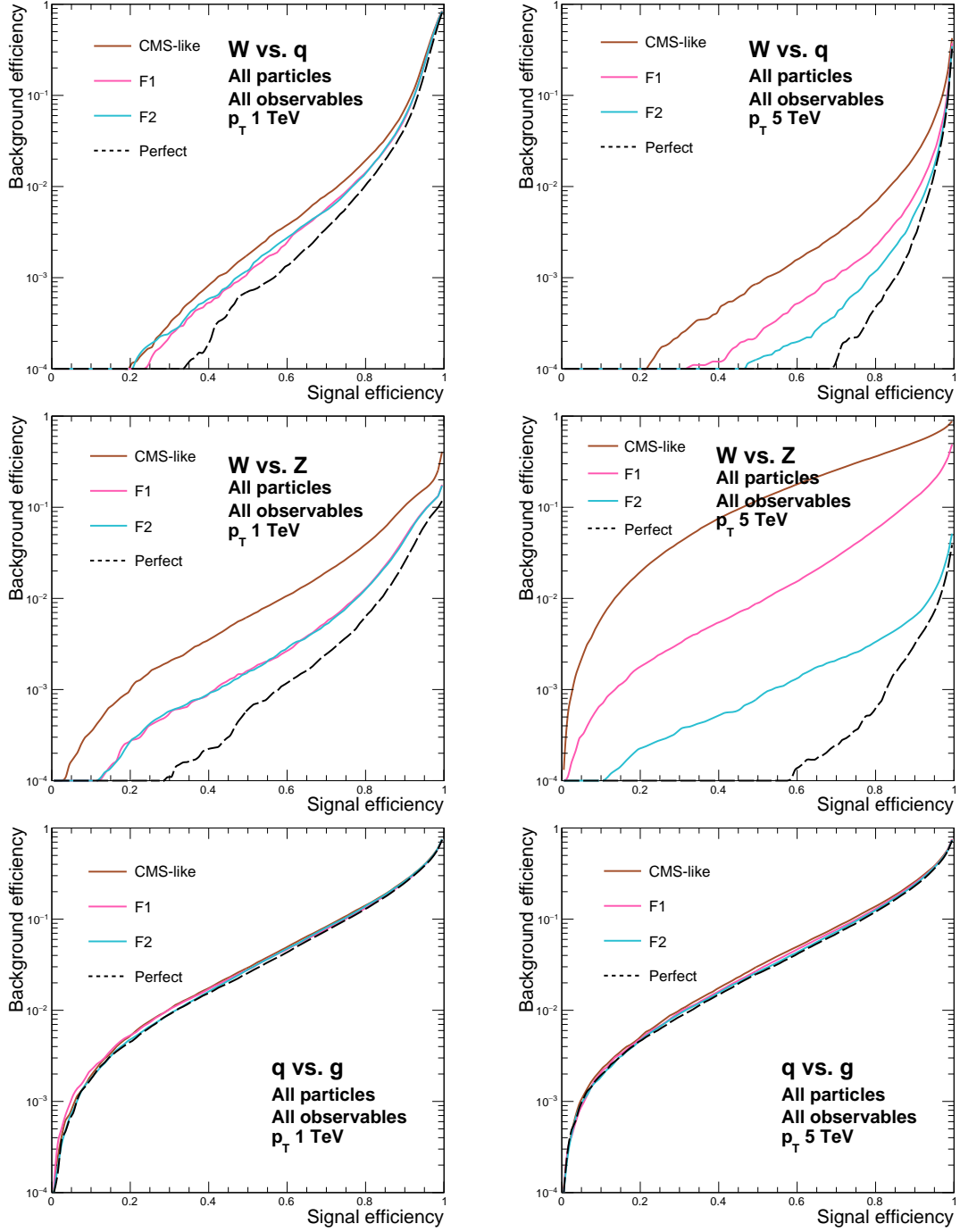


Figure 8: All-particle discrimination performance using realistic detectors. Shown are ROC curves for (top row) W vs. q , (middle row) W vs. Z , and (bottom row) q vs. g discrimination in the (left column) $p_T = 1$ TeV and (right column) $p_T = 5$ TeV bins. The “perfect” detector reference matches the all-particle curves in Figs. 2, 3, and 4.

that any further improvements do not have a corresponding physics gain. The reason this happens is that calorimeter energy resolution (which is assumed to be the same in the F1 and F2 scenarios) also plays a role in discrimination power. This suggests the possibility of jointly optimizing granularity and resolution to achieve balanced jet substructure performance.

4.3 Results using partial information

In some contexts, it may be beneficial to use partial jet information for jet substructure studies, for example using track-only measurements to help mitigate pileup. In Fig. 9, we vary the input particle categories—tracks, tracks+ γ , or all particles—and plot the envelope of the CMS-like, F1 and F2 detector results in the same layout as Fig. 8.

In all cases, as we include more neutral-particle information, we improve (or maintain) discrimination power. As expected from Sec. 3, the gain is minimal (at most a factor of 2) when considering the q vs. g jet discrimination, which relies primarily on jet shape information. For W vs. q and W vs. Z discrimination, adding neutral-particle information greatly improves the discrimination power. The effect is extreme for W vs. Z jets where mass information is dominant and degrading the mass resolution, both through removing neutral-particle information and degrading detector performance, has a very significant impact on the discrimination.

From the size of the envelopes, one can also see that the difference between the CMS-like and F2 performance is most pronounced when all particles are included since those depend on HCAL resolution. When using tracks plus photons, the differences between detector configurations are more modest, suggesting that ECAL granularity is not the primary limiting factor for jet substructure performance.

4.4 Summary of detector study

Finally, we summarize the change in discrimination power as we vary both the particle input categories and detector configurations. Following Eq. (3.1), we define \mathcal{R}_S as the ratio of the background rejection power for two different scenarios for fixed signal efficiency $S\%$.

In Fig. 10, we fix the CMS-like detector configuration and illustrate the gain in background rejection in including more neutral-particle information. The 5×5 grids show \mathcal{R}_{80} (\mathcal{R}_{90}) for 1 (5) TeV on the left (right) for each pairwise comparison of $W/Z/t/q/g$ jets, with (tracks+ γ)/(tracks) in the lower right triangle and (all particle)/(tracks) in the upper left triangle. Comparing to the study in Fig. 5, which assumed a perfect detector, the qualitative features are quite similar. The main difference is that the importance of using all particle information is muted when using a realistic detector compared to a perfect one, but the gains are still substantial. One exception is the W/Z discrimination at 5 TeV where the CMS-like detector is not well-suited to handle such high p_T jets, and we will see benefits below from improved detector granularity and resolution.

In Fig. 11, we consider only all particle information and illustrate the gains in going from a CMS-like detector to an F1 or F2 detector. For the extreme case of W vs. Z jets

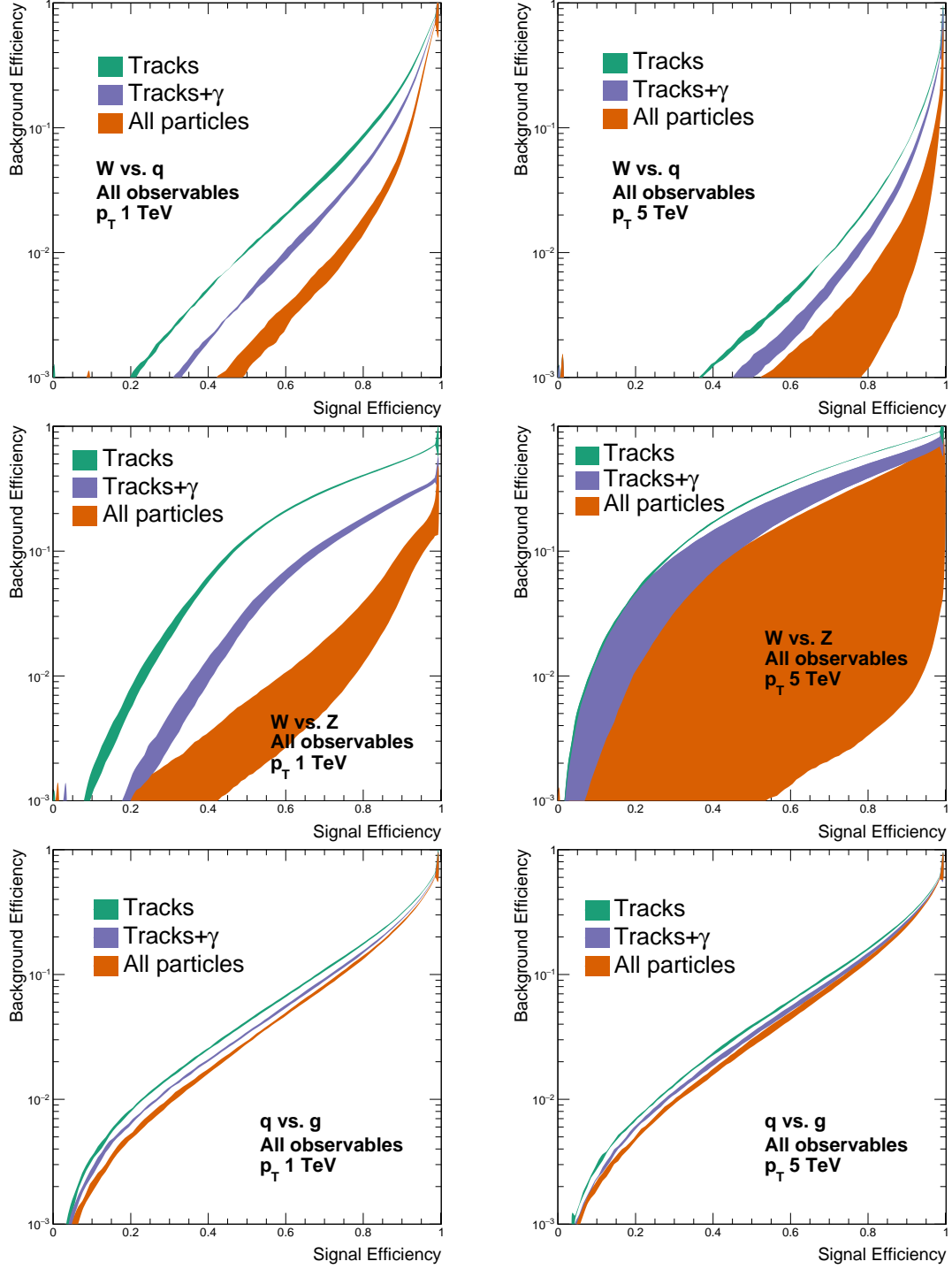


Figure 9: Discrimination performance as the input particles are varied, taking the ROC envelope of the CMS-like, F1, and F2 detector configurations. As in Fig. 8, the layout is (top row) W vs. q , (middle row) W vs. Z , and (bottom row) q vs. g , with (left column) $p_T = 1$ TeV and (right column) $p_T = 5$ TeV.

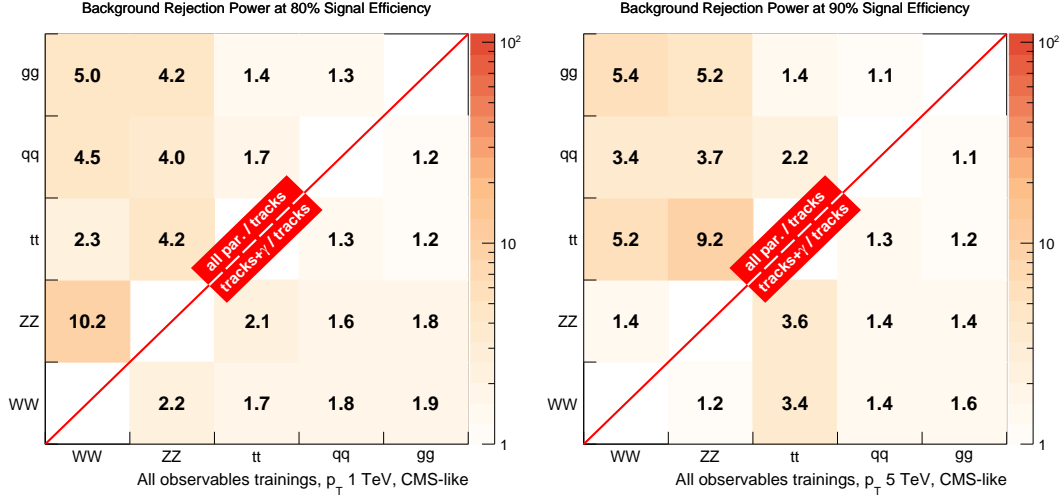


Figure 10: Background rejection ratio (left) \mathcal{R}_{80} for the $p_T = 1$ TeV bin and (right) \mathcal{R}_{90} for the $p_T = 5$ TeV bins, for all pairwise discrimination tasks among $W/Z/t/q/g$ jets using all particle information. This can be compared to Fig. 5, where values in the lower right triangle refer to the ratio (tracks+ γ)/(tracks), while those in the upper left triangle refer to (all particle)/(tracks).

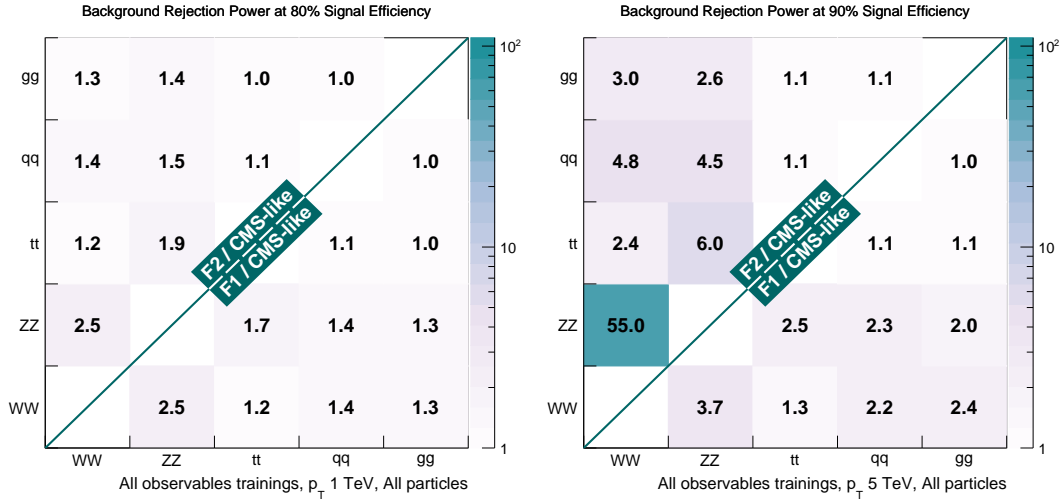


Figure 11: Same as Fig. 10, but using all particle information and showing \mathcal{R}_S values for (Future 2)/(CMS-like) in the upper left triangle and (Future 1)/(CMS-like) in the lower right triangle.

at $p_T = 5$ TeV, the Future 2 detector scenario improves upon the CMS-like scenario by almost two orders of magnitude in background rejection power. This is an extreme example, though any discrimination task involving W/Z identification benefits substantially from the $\text{CMS} \rightarrow \text{F1}$ or $\text{CMS} \rightarrow \text{F2}$ improvement. This example highlights the importance of understanding physical thresholds to achieve major performance improvements and should be a central consideration for future detector research efforts. Since q vs. g discrimination is dominated by shape information, it is not surprising that the future detectors do not offer much performance improvement.

An important note is that top vs. q/g discrimination is not affected much by the detector configuration, as explored further in App. A. This is because the mass information, while dominant, is already maximally discriminant due to the large top mass and is less susceptible to mass resolution effects, as previously discussed in Sec. 3.4. For all tasks, the impact of calorimeter performance is stronger when increasing the jet p_T from 1 TeV (top) to 5 TeV (bottom) because the F1 and F2 detector configurations were selected for their applicability to the higher-energy regime.

5 Conclusions and outlook

Highly-boosted hadronic topologies and jet substructure techniques have proven to be an important part of the LHC physics program, and they will only become more important at future higher-energy experiments. It is therefore vital that we understand how best to utilize current multipurpose detectors, as well as to design new ones. In this paper, we studied the importance of neutral-particle information and calorimetry for jet substructure performance. We used binary BDT classifiers to understand differences in the jet discrimination power achievable in different detector regimes. While recent studies like Refs. [24–26] have focused on the advantages of using track-only information to study boosted scenarios, our results highlight cases where calorimetric information is necessary to maximize physics performance. Using a toy detector simulation with particle-level smearing and discretization tuned for jet substructure performance, we quantified the potential gains from deploying high-resolution calorimetry at a hypothetical future high-energy multi-TeV-scale collider, which could ultimately improve our ability to find new physics. We also explored the intermediate possibility of using tracks plus photons, which recovers a large fraction of the neutral-particle information with reduced demands on calorimeter performance.

By studying the discrimination power between $W/Z/t/q/g$ jets at very high p_T , we were able to disentangle which jet features are required for different jet discrimination tasks. We found that for discrimination based primarily on dimensionless jet shape information, such as q vs. g jets, adding neutral-particle information or improving calorimeter granularity adds very little to performance. When mass resolution is important, such as in W vs. q jets or maximally in W vs. Z jet discrimination, adding neutral-particle information and improving calorimeter granularity are extremely important. For example, in the more typical case of W vs. q jet discrimination, improving the ECAL and HCAL granularity by a factor of 5 or 10

can improve background rejection by a factor of 10 for 5 TeV jets; a similar factor can be lost if one does not include neutral-particle information at all. The effect is even more striking for W vs. Z jet discrimination, which could be a very important tool to characterize potential new physics signals. There, background rejection can be improved by 2 orders of magnitude using all-particle information with the highest granularity calorimetry.

One surprising outcome of this study is that mass resolution does not play as crucial a role for boosted top identification, even though jet mass is a powerful discriminant. This finding is consistent with the conclusions of Ref. [24], but nevertheless highlights the interplay between mass and shape information as well as the impact of signal topology and color structure. Though not part of this study, it would be fruitful to consider reconstructing boosted objects beyond the SM, such as recently explored in Refs. [73–75], which can have different masses, color representations, and decay topologies compared to SM resonances.

In exploring the impact of detector design on jet substructure performance, we have set aside two very important factors: reconstruction feasibility and cost. While there have been studies which explore potential fundamental calorimeter limitations [26], we leave it to other studies such as [67, 76, 77] to determine if high-granularity calorimetry and new reconstruction techniques can deliver even better per-particle separation and performance. This study, emphasizing the effects on physics performance, is meant to be complementary to those detailed reconstruction studies. Assuming that such reconstruction performance can indeed be achieved, we explicitly quantify the physics gains possible from improved calorimetry. Ultimately, one needs to simultaneously optimize cost, feasibility, and physics potential, and the particle physics community needs to decide whether, for example, robust jet discrimination is an important enough goal to drive detector design. Future work may include studies of more detector configurations and higher jet energies. It is also worth considering that, especially in a multivariate context, it may be possible to achieve the same discrimination power using observables with less demanding resolution requirements. In this way, the best balance of cost and performance might be achieved through a combination of track-based, track-plus-photon, and all-particle observables.

Acknowledgements

We thank Sergei Chekanov, Ashutosh Kotwal, Andrew Larkoski, Benjamin Nachman, and Tilman Plehn for useful discussions. The work of M.F. is supported by the U.S. Department of Energy (DOE) under grant contract number DE-SC-00011640. The work of J.T. is supported by the DOE under grant contract number DE-SC-00012567. The work of N.T. and C.V. is supported by Fermi Research Alliance, LLC under Contract No. DE-AC02-07CH11359 with the U.S. Department of Energy, Office of Science, Office of High Energy Physics. A.H. gratefully acknowledges funding in the Emmy-Noether program (HI 1952/1-1) of the German Research Foundation DFG. M.N. and E.C. acknowledge the support of the DOE via the contract DE-SC0010010. E.C. was partially supported by a Karen T. Romer Undergraduate Teaching and Research Award through Brown University.

A Top jets vs. gluon jets

A surprising outcome of this study is that mass resolution does not play as dominant a role for top jet vs. g jet separation as it does for, say, W jet vs. g jet separation. We can see this in Fig. 12, which shows the m_{mMDT} and $\tau_{32}^{\beta=1}$ distributions for different detector configurations and particle categories. Compared to the W vs. g case in Fig. 6, the signal/background separation in the top vs. g case is more stable as the detector configuration changes. Similarly, in the ROC curves in Fig. 13, there is relatively little spread in the performance as the amount of neutral and calorimeter information is varied.

It is important to emphasize that the mass resolution for top jets does degrade as neutral-particle information is lost. The point made in Secs. 3.4 and 4.4 is that the *separation* of the observable distributions is not heavily impacted by the degree of neutral-particle information, yielding values of \mathcal{R}_S in Fig. 5 that are always less than 1.5 for (tracks+ γ)/(tracks) and (all particles)/(tracks). In this sense, the discrimination power offered by mass observables is maximal for top quarks, even as the mass resolution degrades.

References

- [1] CMS collaboration, S. Chatrchyan et al., *The CMS Experiment at the CERN LHC*, [*JINST* **3** \(2008\) S08004](#).
- [2] ATLAS collaboration, G. Aad et al., *The ATLAS Experiment at the CERN Large Hadron Collider*, [*JINST* **3** \(2008\) S08003](#).
- [3] M. H. Seymour, *Tagging a heavy Higgs boson*, in *ECFA Large Hadron Collider Workshop, Aachen, Germany, 4-9 Oct 1990: Proceedings.2.*, pp. 557–569, 1991.
- [4] M. H. Seymour, *Searches for new particles using cone and cluster jet algorithms: A Comparative study*, [*Z. Phys.* **C62** \(1994\) 127–138](#).
- [5] J. M. Butterworth, B. E. Cox and J. R. Forshaw, *WW scattering at the CERN LHC*, [*Phys. Rev.* **D65** \(2002\) 096014](#), [[hep-ph/0201098](#)].
- [6] J. M. Butterworth, J. R. Ellis and A. R. Raklev, *Reconstructing sparticle mass spectra using hadronic decays*, [*JHEP* **05** \(2007\) 033](#), [[hep-ph/0702150](#)].
- [7] J. M. Butterworth, A. R. Davison, M. Rubin and G. P. Salam, *Jet substructure as a new Higgs search channel at the LHC*, [*Phys. Rev. Lett.* **100** \(2008\) 242001](#), [[0802.2470](#)].
- [8] A. Abdesselam et al., *Boosted objects: A Probe of beyond the Standard Model physics*, [*Eur. Phys. J.* **C71** \(2011\) 1661](#), [[1012.5412](#)].
- [9] A. Altheimer et al., *Jet Substructure at the Tevatron and LHC: New results, new tools, new benchmarks*, [*J. Phys.* **G39** \(2012\) 063001](#), [[1201.0008](#)].
- [10] A. Altheimer et al., *Boosted objects and jet substructure at the LHC. Report of BOOST2012, held at IFIC Valencia, 23rd-27th of July 2012*, [*Eur. Phys. J.* **C74** \(2014\) 2792](#), [[1311.2708](#)].
- [11] D. Adams et al., *Towards an Understanding of the Correlations in Jet Substructure*, [*Eur. Phys. J.* **C75** \(2015\) 409](#), [[1504.00679](#)].

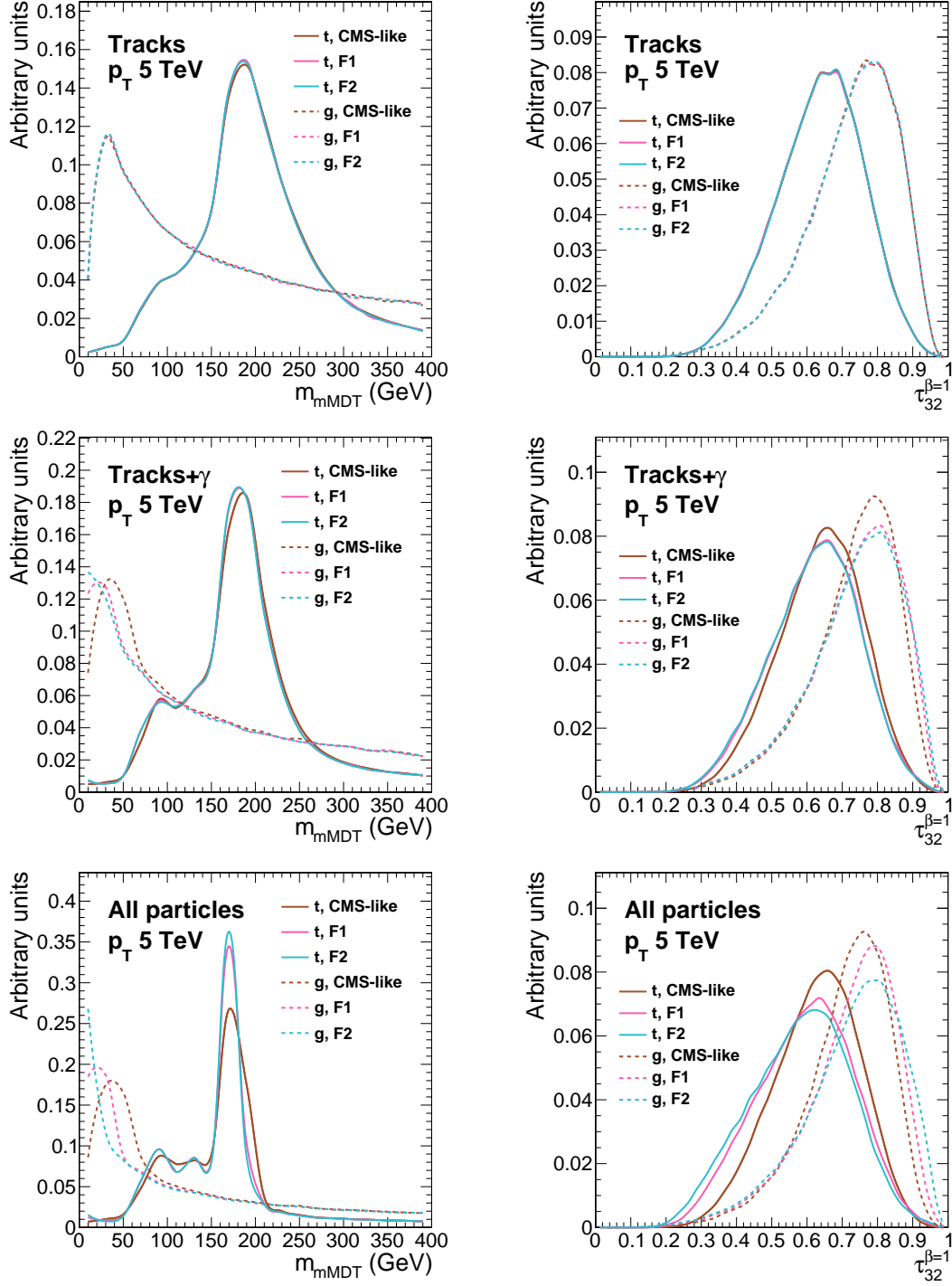


Figure 12: Same layout as Fig. 6 but now comparing top jets to gluon jets with (left column) m_{mMDT} and (right column) $\tau_{32}^{\beta=1}$.

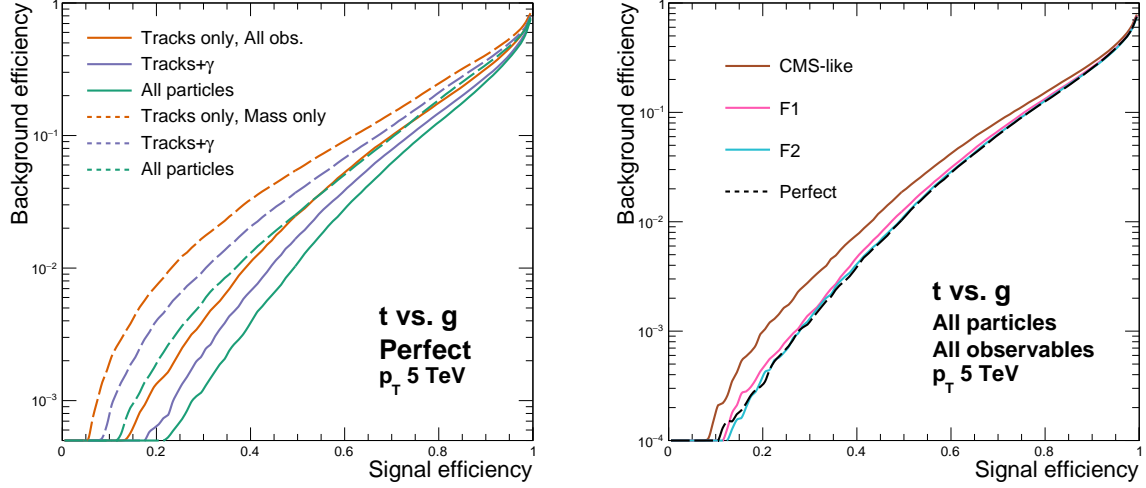


Figure 13: ROC discrimination curves for top vs. gluon discrimination in the $p_T = 5$ TeV bin. The left panel for a perfect detector has the same format as Fig. 2, and the right panel for realistic detectors has the same format as Fig. 8.

- [12] A. J. Larkoski, I. Moult and B. Nachman, *Jet Substructure at the Large Hadron Collider: A Review of Recent Advances in Theory and Machine Learning*, [1709.04464](#).
- [13] ATLAS collaboration, G. Aad et al., *Light-quark and gluon jet discrimination in pp collisions at $\sqrt{s} = 7$ TeV with the ATLAS detector*, *Eur. Phys. J.* **C74** (2014) 3023, [[1405.6583](#)].
- [14] ATLAS collaboration, G. Aad et al., *Measurement of jet charge in dijet events from $\sqrt{s}=8$ TeV pp collisions with the ATLAS detector*, *Phys. Rev.* **D93** (2016) 052003, [[1509.05190](#)].
- [15] ATLAS collaboration, *Search for resonances with boson-tagged jets in 15.5 fb^{-1} of pp collisions at $\sqrt{s} = 13$ TeV collected with the ATLAS detector*, Tech. Rep. ATLAS-CONF-2016-055, CERN, Geneva, Aug, 2016.
- [16] ATLAS collaboration, G. Aad et al., *Measurement of the charged-particle multiplicity inside jets from $\sqrt{s} = 8$ TeV pp collisions with the ATLAS detector*, *Eur. Phys. J.* **C76** (2016) 322, [[1602.00988](#)].
- [17] ATLAS collaboration, T. A. collaboration, *Jet mass reconstruction with the ATLAS Detector in early Run 2 data*, tech. rep., 2016.
- [18] ATLAS collaboration, T. A. collaboration, *Discrimination of Light Quark and Gluon Jets in pp collisions at $\sqrt{s} = 8$ TeV with the ATLAS Detector*, .
- [19] D. Krohn, M. D. Schwartz, T. Lin and W. J. Waalewijn, *Jet Charge at the LHC*, *Phys. Rev. Lett.* **110** (2013) 212001, [[1209.2421](#)].
- [20] W. J. Waalewijn, *Calculating the Charge of a Jet*, *Phys. Rev.* **D86** (2012) 094030, [[1209.3019](#)].
- [21] H.-M. Chang, M. Procura, J. Thaler and W. J. Waalewijn, *Calculating Track Thrust with Track Functions*, *Phys. Rev.* **D88** (2013) 034030, [[1306.6630](#)].

- [22] H.-M. Chang, M. Procura, J. Thaler and W. J. Waalewijn, *Calculating Track-Based Observables for the LHC*, *Phys. Rev. Lett.* **111** (2013) 102002, [[1303.6637](#)].
- [23] S. Schaetzel and M. Spannowsky, *Tagging highly boosted top quarks*, *Phys. Rev.* **D89** (2014) 014007, [[1308.0540](#)].
- [24] A. J. Larkoski, F. Maltoni and M. Selvaggi, *Tracking down hyper-boosted top quarks*, *JHEP* **06** (2015) 032, [[1503.03347](#)].
- [25] M. Spannowsky and M. Stoll, *Tracking New Physics at the LHC and beyond*, *Phys. Rev.* **D92** (2015) 054033, [[1505.01921](#)].
- [26] S. Bressler, T. Flacke, Y. Kats, S. J. Lee and G. Perez, *Hadronic Calorimeter Shower Size: Challenges and Opportunities for Jet Substructure in the Superboosted Regime*, *Phys. Lett.* **B756** (2016) 137–141, [[1506.02656](#)].
- [27] ALEPH collaboration, D. Buskulic et al., *Performance of the ALEPH detector at LEP*, *Nucl. Instrum. Meth.* **A360** (1995) 481–506.
- [28] CMS collaboration, A. M. Sirunyan et al., “Particle-flow reconstruction and global event description with the CMS detector.” 2017.
- [29] ATLAS collaboration, M. Aaboud et al., *Jet reconstruction and performance using particle flow with the ATLAS Detector*, *Eur. Phys. J.* **C77** (2017) 466, [[1703.10485](#)].
- [30] J. Alwall, R. Frederix, S. Frixione, V. Hirschi, F. Maltoni, O. Mattelaer et al., *The automated computation of tree-level and next-to-leading order differential cross sections, and their matching to parton shower simulations*, *JHEP* **07** (2014) 079, [[1405.0301](#)].
- [31] R. D. Ball et al., *Parton distributions with LHC data*, *Nucl. Phys.* **B867** (2013) 244–289, [[1207.1303](#)].
- [32] T. Sjöstrand, S. Ask, J. R. Christiansen, R. Corke, N. Desai, P. Ilten et al., *An Introduction to PYTHIA 8.2*, *Comput. Phys. Commun.* **191** (2015) 159–177, [[1410.3012](#)].
- [33] P. Skands, S. Carrazza and J. Rojo, *Tuning PYTHIA 8.1: the Monash 2013 Tune*, *Eur. Phys. J.* **C74** (2014) 3024, [[1404.5630](#)].
- [34] M. Cacciari, G. P. Salam and G. Soyez, *Fastjet user manual*, *Eur. Phys. J.* **C72** (2012) 1896, [[1111.6097](#)].
- [35] M. Cacciari and G. P. Salam, *Dispelling the n^3 myth for the k_t jet-finder*, *Phys. Lett.* **B641** (2006) 57–61, [[hep-ph/0512210](#)].
- [36] M. Cacciari, G. P. Salam and G. Soyez, *The Anti- $k(t)$ jet clustering algorithm*, *JHEP* **04** (2008) 063, [[0802.1189](#)].
- [37] J. Dolen, P. Harris, S. Marzani, S. Rappoccio and N. Tran, *Thinking outside the ROCs: Designing Decorrelated Taggers (DDT) for jet substructure*, *JHEP* **05** (2016) 156, [[1603.00027](#)].
- [38] C. Shimmin, P. Sadowski, P. Baldi, E. Weik, D. Whiteson, E. Goul et al., *Decorrelated Jet Substructure Tagging using Adversarial Neural Networks*, [1703.03507](#).
- [39] D. Krohn, J. Thaler and L.-T. Wang, *Jet Trimming*, *JHEP* **02** (2010) 084, [[0912.1342](#)].
- [40] S. D. Ellis, C. K. Vermilion and J. R. Walsh, *Recombination Algorithms and Jet Substructure: Pruning as a Tool for Heavy Particle Searches*, *Phys. Rev.* **D81** (2010) 094023, [[0912.0033](#)].

- [41] M. Dasgupta, A. Fregoso, S. Marzani and G. P. Salam, *Towards an understanding of jet substructure*, *JHEP* **09** (2013) 029, [[1307.0007](#)].
- [42] A. J. Larkoski, S. Marzani, G. Soyez and J. Thaler, *Soft Drop*, *JHEP* **05** (2014) 146, [[1402.2657](#)].
- [43] J. Thaler and K. Van Tilburg, *Identifying Boosted Objects with N -subjettiness*, *JHEP* **03** (2011) 015, [[1011.2268](#)].
- [44] P. Gras, S. Höche, D. Kar, A. Larkoski, L. Lönnblad, S. Plätzer et al., *Systematics of quark/gluon tagging*, *JHEP* **07** (2017) 091, [[1704.03878](#)].
- [45] J. Thaler and K. Van Tilburg, *Maximizing Boosted Top Identification by Minimizing N -subjettiness*, *JHEP* **02** (2012) 093, [[1108.2701](#)].
- [46] A. J. Larkoski, G. P. Salam and J. Thaler, *Energy Correlation Functions for Jet Substructure*, *JHEP* **06** (2013) 108, [[1305.0007](#)].
- [47] A. J. Larkoski, I. Moult and D. Neill, *Analytic Boosted Boson Discrimination*, *JHEP* **05** (2016) 117, [[1507.03018](#)].
- [48] I. Moult, L. Necib and J. Thaler, *New Angles on Energy Correlation Functions*, *JHEP* **12** (2016) 153, [[1609.07483](#)].
- [49] F. Pandolfi and D. Del Re, *Search for the Standard Model Higgs Boson in the $H \rightarrow ZZ \rightarrow l^+ l^- q \bar{q}$ Decay Channel at CMS*, 2013.
- [50] CMS collaboration, S. Chatrchyan et al., *Search for a Higgs boson in the decay channel H to $ZZ(*)$ to $q \bar{q} \ell^+ \ell^-$ in pp collisions at $\sqrt{s} = 7$ TeV*, *JHEP* **04** (2012) 036, [[1202.1416](#)].
- [51] A. J. Larkoski, I. Moult and D. Neill, *Building a Better Boosted Top Tagger*, *Phys. Rev.* **D91** (2015) 034035, [[1411.0665](#)].
- [52] A. J. Larkoski, J. Thaler and W. J. Waalewijn, *Gaining (Mutual) Information about Quark/Gluon Discrimination*, *JHEP* **11** (2014) 129, [[1408.3122](#)].
- [53] J. Gallicchio and M. D. Schwartz, *Quark and Gluon Tagging at the LHC*, *Phys. Rev. Lett.* **107** (2011) 172001, [[1106.3076](#)].
- [54] J. Gallicchio and M. D. Schwartz, *Quark and Gluon Jet Substructure*, *JHEP* **04** (2013) 090, [[1211.7038](#)].
- [55] G. P. Salam, L. Schunk and G. Soyez, *Dichroic subjettiness ratios to distinguish colour flows in boosted boson tagging*, *JHEP* **03** (2017) 022, [[1612.03917](#)].
- [56] A. Hoecker, P. Speckmayer, J. Stelzer, J. Therhaag, E. von Toerne and H. Voss, *TMVA: Toolkit for Multivariate Data Analysis*, *PoS ACAT* (2007) 040, [[physics/0703039](#)].
- [57] J. H. Friedman, *Greedy function approximation: A gradient boosting machine*, *Annals of Statistics* **29** (2000) 1189–1232.
- [58] L. de Oliveira, M. Kagan, L. Mackey, B. Nachman and A. Schwartzman, *Jet-images ? deep learning edition*, *JHEP* **07** (2016) 069, [[1511.05190](#)].
- [59] P. Baldi, K. Bauer, C. Eng, P. Sadowski and D. Whiteson, *Jet Substructure Classification in High-Energy Physics with Deep Neural Networks*, *Phys. Rev.* **D93** (2016) 094034, [[1603.09349](#)].

- [60] K. Datta and A. Larkoski, *How Much Information is in a Jet?*, *JHEP* **06** (2017) 073, [[1704.08249](#)].
- [61] A. J. Larkoski, I. Moult and D. Neill, *Power Counting to Better Jet Observables*, *JHEP* **12** (2014) 009, [[1409.6298](#)].
- [62] CMS collaboration, *V Tagging Observables and Correlations*, Tech. Rep. CMS-PAS-JME-14-002, CERN, Geneva, 2014.
- [63] CMS collaboration, *CMS Technical Design Report for HL-LHC*, Tech. Rep. CMS-TDR-17-001, CERN, 2017. Geneva, 2017.
- [64] CMS collaboration, *Jet algorithms performance in 13 TeV data*, Tech. Rep. CMS-PAS-JME-16-003, CERN, Geneva, 2017.
- [65] CMS collaboration, V. Khachatryan et al., *Identification techniques for highly boosted W bosons that decay into hadrons*, *JHEP* **12** (2014) 017, [[1410.4227](#)].
- [66] CMS collaboration, A. M. Sirunyan et al., *Search for massive resonances decaying into WW, WZ or ZZ bosons in proton-proton collisions at $\sqrt{s} = 13$ TeV*, *JHEP* **03** (2017) 162, [[1612.09159](#)].
- [67] S. V. Chekanov, M. Beydler, A. V. Kotwal, L. Gray, S. Sen, N. V. Tran et al., *Initial performance studies of a general-purpose detector for multi-TeV physics at a 100 TeV pp collider*, *JINST* **12** (2017) P06009, [[1612.07291](#)].
- [68] D. Krohn, M. D. Schwartz, M. Low and L.-T. Wang, *Jet Cleansing: Pileup Removal at High Luminosity*, *Phys. Rev.* **D90** (2014) 065020, [[1309.4777](#)].
- [69] D. Bertolini, P. Harris, M. Low and N. Tran, *Pileup per particle identification*, *JHEP* **10** (2014) 059, [[1407.6013](#)].
- [70] M. Cacciari, G. P. Salam and G. Soyez, *SoftKiller, a particle-level pileup removal method*, *Eur. Phys. J.* **C75** (2015) 59, [[1407.0408](#)].
- [71] G. Soyez, G. P. Salam, J. Kim, S. Dutta and M. Cacciari, *Pileup subtraction for jet shapes*, *Phys. Rev. Lett.* **110** (2013) 162001, [[1211.2811](#)].
- [72] P. T. Komiske, E. M. Metodiev, B. Nachman and M. D. Schwartz, *Pileup Mitigation with Machine Learning (PUMML)*, [1707.08600](#).
- [73] J. A. Aguilar-Saavedra, *Stealth multiboson signals*, [1705.07885](#).
- [74] CMS collaboration, A. M. Sirunyan et al., *Search for low mass vector resonances decaying to quark-antiquark pairs in proton-proton collisions at $\sqrt{s} = 13$ TeV*, [1705.10532](#).
- [75] J. A. Aguilar-Saavedra, J. H. Collins and R. K. Mishra, *A generic anti-QCD jet tagger*, [1709.01087](#).
- [76] S. Chekanov et al., “A high granularity hadronic calorimeter for multi TeV jets.” FCC Week 2017, <https://indico.cern.ch/event/556692/contributions/2592529>, 2017.
- [77] S. Chekanov et al., “Simulations of detector response for multi-TeV physics at a 100 TeV pp collider.” Boost 2017 Conference, <https://indico.cern.ch/event/579660/contributions/2575089>, 2017.